

# Quantum teleportation with full Bell-basis detection between a $^{40}\text{Ca}^+$ ion and a single photon

Elena Arenskötter, Stephan Kucera, Omar Elshehy, Max Bergerhoff, Matthias Kreis, and Jürgen Eschner\*  
*Experimentalphysik, Universität des Saarlandes, 66123 Saarbrücken, Germany*  
(Dated: January 27, 2023)

We present several interface protocols between a single trapped atom and single photons from an entangled-pair source, among them the quantum teleportation of a qubit state from a single trapped  $^{40}\text{Ca}^+$  ion onto a single photon. As appropriate Bell measurement, the teleportation protocol employs heralded absorption of one photon of the polarisation-entangled pair, which allows us to identify all four Bell states. Further protocols enabled by heralded absorption comprise quantum state mapping from a single photon to a single ion and transfer of polarization entanglement of a photon pair to entanglement between a single ion and the partner photon.

Quantum networks with trapped ions [1, 2] require interfaces between ion-based nodes and photon-based channels and a resource of entanglement for long-distance communication [3]. Photon-pair sources based on spontaneous parametric down-conversion (SPDC) serve as such a resource of entanglement, as they can be matched in frequency and bandwidth to the ionic transitions [4–7]. When entanglement between distant nodes has been established, quantum teleportation [8] provides a suitable protocol, alternative to direct transmission, for quantum state transfer [9].

Application of teleportation has been shown between photons over large distances [10–15], between quantum nodes [16–20], and from a photon to a quantum node [21–24]. In this paper we show quantum teleportation of an atomic qubit, encoded in the Zeeman sub-levels of the  $^{40}\text{Ca}^+$  ion, to the polarisation qubit of a single 854 nm photon. The teleportation protocol employs heralded absorption of a single photon by the ion [4, 9, 25, 26], which functions as a Bell measurement. In contrast to photonic teleportation protocols, this Bell measurement can identify all four Bell states. Before we proceed to the full teleportation protocol, we demonstrate more elementary interface operations between single photons from an SPDC source and a single ion. We demonstrate heralded quantum state mapping from a single-photon polarization qubit onto the ground-state Zeeman qubit of the  $^{40}\text{Ca}^+$  ion, which was previously demonstrated with laser photons [27], and we apply this protocol to implement the transfer of entanglement from photon-photon to atom-photon qubit pairs.

## EXPERIMENTAL SETUP

Figure 1 shows the experimental setup. A single  $^{40}\text{Ca}^+$  ion is trapped in a linear Paul trap with single-photon optical access by two in-vacuum high-numerical-aperture laser objectives (HALOs, NA = 0.4). One of the objectives is used to focus 854 nm photons onto the ion, in order to excite it from its initial state in the  $D_{5/2}$  manifold to the  $P_{3/2}$  manifold. The second HALO is used

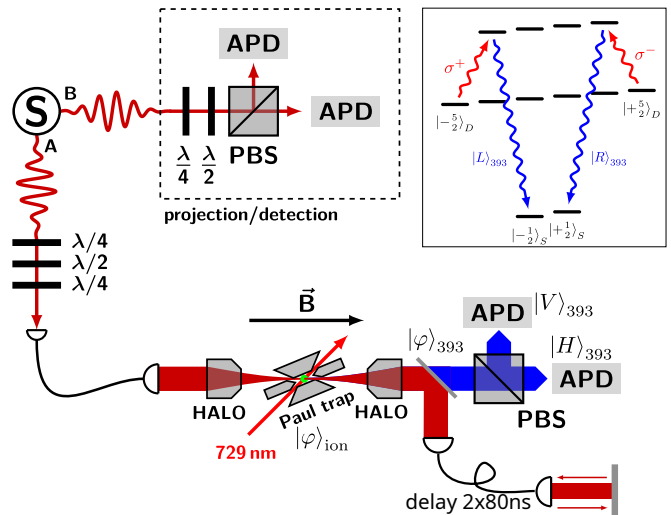


FIG. 1. Schematic of the experiment. The photon-pair source S generates polarization-entangled photon pairs. Photons in output A are directed to the atomic setup, where a single trapped  $^{40}\text{Ca}^+$  ion acts as a quantum node. The photons pass a set of waveplates to compensate for polarization rotations in the fiber connecting the photons to the atomic setup. The partner photons in output B are sent to a tomography setup for analyzing their quantum state. The inset shows the relevant energy levels employed in the protocols.

to collect the emitted (Raman-scattered) 393 nm photons which are subsequently polarisation-projected with a Wollaston prism (PBS), and detected with free-space coupled APDs in both outputs. This HALO is also used to couple the non-absorbed 854 nm photons into a 16 m long single-mode fiber with attached retroreflector. The fiber is used to create 160 ns delay and an inversion of the direction relative to the quantization axis, which is defined by a magnetic field of 2.855 G. The inset shows the relevant energy levels and Zeeman sublevels of the  $^{40}\text{Ca}^+$  ion, as they are employed in the protocols.

The entanglement resource, marked as S, produces frequency-stable polarization-entangled photon pairs at 854 nm in a cavity enhanced spontaneous-parametric-down-conversion process (SPDC) with interferometric

configuration. We refer to [28] for more detailed information. The photon in output A has a linewidth of 12.29 MHz and is tuned to be resonant with the 22 MHz-linewidth  $D_{5/2}$ - $P_{3/2}$  transition of the  $^{40}\text{Ca}^+$  ion. Output B is detuned by 480 MHz. The result of a tomographic measurement [29] on the photon-pair state  $\rho$  in the fiber-coupled outputs A and B is shown in figure 2. A fidelity of  $\langle \Psi^- | \rho | \Psi^- \rangle = 91.64(2)\%$  (97.16(2)% with background correction) with the antisymmetric Bell state, and a purity of  $\text{tr}(\rho^2) = 84.97(4)\%$  (95.21(3)% with background correction) are measured at our operating conditions (15 mW of pump light at 427 nm). Background originates from lost-partner events and detector dark counts; see [28] for more information. A fiber-coupled pair rate of  $2.69 \times 10^5 \text{ s}^{-1}$  in the output fibers A and B is inferred from the correlation measurements.

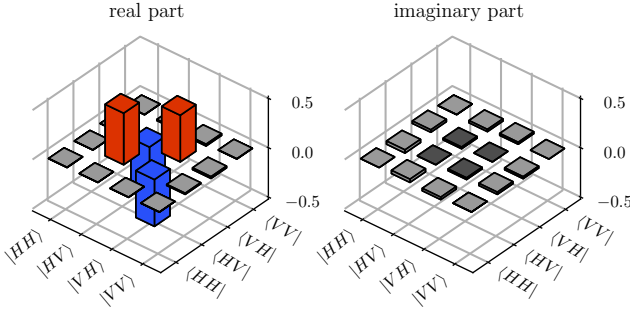


FIG. 2. Real and imaginary part of the photon-photon density matrix, reconstructed with maximum likelihood quantum state tomography.

## ENTANGLEMENT TRANSFER

The protocol for photon-to-atom state-mapping is similar to [9, 30] and adapted to the experimental setup shown in figure 1. We use the abbreviations  $|\pm 1/2\rangle_S = |\text{S}_{1/2}, m = \pm 1/2\rangle$  and  $|\pm 5/2\rangle_D = |\text{D}_{5/2}, m = \pm 5/2\rangle$  for the atomic states and  $|R\rangle/|L\rangle$  ( $|H\rangle/|V\rangle$ ) for the single-photon states in the circular (linear) polarization modes. The protocol starts by preparing a coherent superposition in  $\text{D}_{5/2}$ ,  $|\varphi\rangle_D = \frac{1}{\sqrt{2}} (| -5/2 \rangle_D + e^{i\phi} | +5/2 \rangle_D)$ , then the photon-pair generation is switched on with an acousto-optic modulator that controls the SPDC pump laser. Photons from arm A are focused onto to the ion, co-propagating with the direction of the magnetic field. The absorption of a 854 nm (red) photon in the polarization qubit state

$$|\varphi\rangle_A = a|R\rangle_A + b|L\rangle_A \quad (1)$$

with the amplitudes  $a$  and  $b$  releases with high probability (93.5%) a 393 nm (blue) Raman photon in the state  $|\varphi\rangle_{393}$ . If the red photon is not absorbed in the first passage, it is collected and sent back to the ion with a time

delay of 160 ns, now counter-propagating to the magnetic field. First and second absorption are distinguished by the delay of the detected 393 nm photon with respect to the partner photon in arm B. The Raman scattering process is described by the operators

$$\hat{R}_{A,D}^{1\text{st}} = |L\rangle_{393} | -1/2 \rangle_S \langle R|_A \langle -5/2 |_D + |R\rangle_{393} | +1/2 \rangle_S \langle L|_A \langle +5/2 |_D \quad (2)$$

$$\hat{R}_{A,D}^{2\text{nd}} = |L\rangle_{393} | -1/2 \rangle_S \langle L|_A \langle -5/2 |_D + |R\rangle_{393} | +1/2 \rangle_S \langle R|_A \langle +5/2 |_D \quad (3)$$

for the first and second passage, respectively. Projecting  $|\varphi\rangle_{393}$  onto

$$|H\rangle_{393} = \frac{|R\rangle_{393} + |L\rangle_{393}}{\sqrt{2}} \quad |V\rangle_{393} = \frac{|R\rangle_{393} - |L\rangle_{393}}{i\sqrt{2}} \quad (4)$$

completes the state-mapping process to the atomic ground state qubit, which is now described by

$$|\varphi\rangle_S^{1\text{st}} = \frac{1}{\sqrt{2}} (a | -1/2 \rangle_S \pm b | +1/2 \rangle_S) \quad (5)$$

$$|\varphi\rangle_S^{2\text{nd}} = \frac{1}{\sqrt{2}} (b | -1/2 \rangle_S \pm a | +1/2 \rangle_S) \quad (6)$$

for the first and second passage. The  $\pm$  sign corresponds to the  $|H\rangle_{393}$  and  $|V\rangle_{393}$  projection results of the 393 nm photon, which also heralds the absorption and thereby allows us to filter out successful mapping processes. The fidelity of the mapping was measured to be  $\chi_{11} = 96.2\%$ , allowing an exposure time of 56  $\mu\text{s}$  for detecting a coincidence between heralding photon and partner photon (arm B); see Supplement for more information. Magnetic field fluctuations are the main limitation to the fidelity. To counteract phase fluctuations in the atomic qubit due to magnetic stray fields, a spin-echo sequence synchronised with the Larmor precession is applied in the following measurements (see Methods).

The photon-to-atom state mapping protocol is now applied to realise the transfer of polarization entanglement from the two-photon state to the atom-photon state. Using all heralded absorption events, full quantum state tomography is performed on the two-qubit state of atom in  $\text{S}_{1/2}$  and 393-nm photon (see Supplement). It reveals the reconstructed density matrices displayed in figure 3. The overlap fidelities and purities of the reconstructed state with the maximally entangled state  $|\Psi^-\rangle$  (c.f. eq. (8)) are summarized in table I. Background correction accounts for false coincidence events inherent in the SPDC process, for details see [31]. We also correct for the contrast reduction resulting from the binning in the data processing, see supplement.

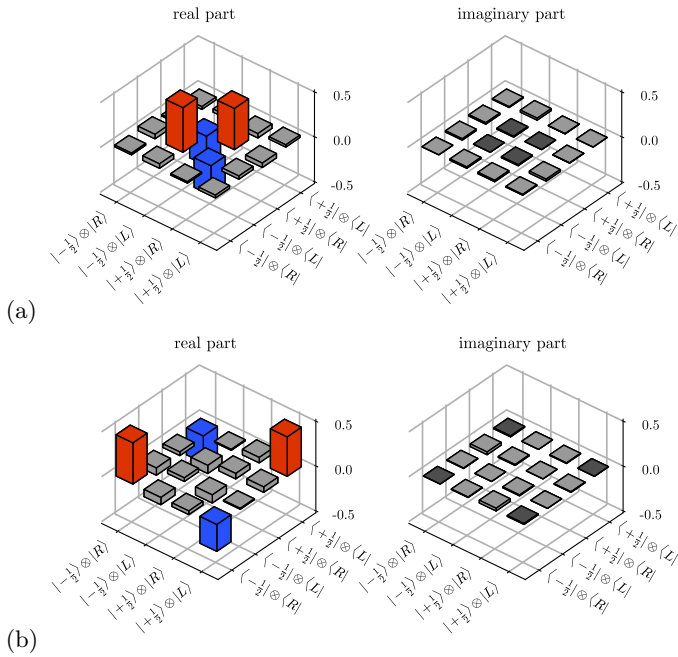


FIG. 3. Real and imaginary parts of the density matrices of the reconstructed atom-photon state for heralded absorption in the first (a) and second passage (b). Background and binning correction is applied.

TABLE I. Fidelities and purities of the entanglement transfer. The values in brackets are corrected for background and binning.

	first passage	second passage
$\langle \Psi^-   \rho   \Psi^- \rangle$	78.0(9) % (82.4(10) %)	52(1) % (76(2) %)
$\text{tr}(\rho^2)$	65(1) % (72(1) %)	36(1) % (64(5) %)

## QUANTUM STATE TELEPORTATION

Atom-to-photon quantum state teleportation starts with a qubit encoded in the  $D_{5/2}$  manifold,

$$|\varphi\rangle_D = \alpha | -5/2 \rangle_D + \beta | +5/2 \rangle_D \quad (7)$$

and the entangled two-photon state  $|\Psi^-\rangle_{A,B}$ . The Bell states between the 854 nm photon in arm A and the atom in  $D_{5/2}$  are defined by

$$\begin{aligned} |\Phi^\pm\rangle_{A,D} &= \frac{1}{\sqrt{2}} (|R\rangle_A | -5/2 \rangle_D \pm |L\rangle_A | +5/2 \rangle_D) \\ |\Psi^\pm\rangle_{A,D} &= \frac{1}{\sqrt{2}} (|R\rangle_A | +5/2 \rangle_D \pm |L\rangle_A | -5/2 \rangle_D) \end{aligned} \quad (8)$$

The joint state in the standard teleportation notation [8] is then

$$\begin{aligned} |\Psi^-\rangle_{A,B} \otimes |\varphi\rangle_D &= \frac{1}{2} \left( \begin{aligned} &(\alpha |R\rangle_B - \beta |L\rangle_B) \otimes |\Psi^+\rangle_{A,D} \\ &-(\alpha |R\rangle_B + \beta |L\rangle_B) \otimes |\Psi^-\rangle_{A,D} \\ &+(\beta |R\rangle_B - \alpha |L\rangle_B) \otimes |\Phi^+\rangle_{A,D} \\ &-(\beta |R\rangle_B + \alpha |L\rangle_B) \otimes |\Phi^-\rangle_{A,D} \end{aligned} \right) \end{aligned}$$

The Bell state measurement on the atom and the photon in arm A, as required for the teleportation, is performed by the heralded absorption process and subsequent projection of the 393 nm Raman photon onto the linear polarizations of eq. (4) and projection of the  $S_{1/2}$  qubit state onto the superpositions of the Zeeman sub-levels

$$|+\rangle_S = \frac{| -1/2 \rangle_S + | +1/2 \rangle_S}{\sqrt{2}} \quad |-\rangle_S = \frac{| -1/2 \rangle_S - | +1/2 \rangle_S}{i\sqrt{2}}$$

This is understood by describing the eight possible measurement outcomes – herald projection, atomic ground state projection, and absorption in first or second passage – with the help of the Raman process operators for the first and second passage (eq. (2), eq. (3))

$$\begin{aligned} (\langle H |_{393} \langle + |_S) \hat{R}_{A,D}^{1^{\text{st}}} &= \frac{1}{\sqrt{2}} \langle \Phi^+ |_{A,D} \\ (\langle V |_{393} \langle - |_S) \hat{R}_{A,D}^{1^{\text{st}}} &= \frac{1}{\sqrt{2}} \langle \Phi^+ |_{A,D} \end{aligned} \quad (9)$$

$$\begin{aligned} (\langle H |_{393} \langle - |_S) \hat{R}_{A,D}^{1^{\text{st}}} &= \frac{i}{\sqrt{2}} \langle \Phi^- |_{A,D} \\ (\langle V |_{393} \langle + |_S) \hat{R}_{A,D}^{1^{\text{st}}} &= \frac{-i}{\sqrt{2}} \langle \Phi^- |_{A,D} \end{aligned} \quad (10)$$

$$\begin{aligned} (\langle H |_{393} \langle + |_S) \hat{R}_{A,D}^{2^{\text{nd}}} &= \frac{1}{\sqrt{2}} \langle \Psi^+ |_{A,D} \\ (\langle V |_{393} \langle - |_S) \hat{R}_{A,D}^{2^{\text{nd}}} &= \frac{1}{\sqrt{2}} \langle \Psi^+ |_{A,D} \end{aligned} \quad (11)$$

$$\begin{aligned} (\langle H |_{393} \langle - |_S) \hat{R}_{A,D}^{2^{\text{nd}}} &= \frac{i}{\sqrt{2}} \langle \Psi^- |_{A,D} \\ (\langle V |_{393} \langle + |_S) \hat{R}_{A,D}^{2^{\text{nd}}} &= \frac{-i}{\sqrt{2}} \langle \Psi^- |_{A,D} \end{aligned} \quad (12)$$

One sees that we project onto the  $|\Phi^\pm\rangle_{A,D}$  states in the first passage and onto the  $|\Psi^\pm\rangle_{A,D}$  states in the second passage, hence all four Bell states are detected. The result of the projection measurement is the classical information that completes the quantum state teleportation onto photon B.

To demonstrate the teleportation of various input qubit states, we prepare the atomic basis states  $| -5/2 \rangle_D$ ,  $| +5/2 \rangle_D$ , and various superpositions

TABLE II. Process fidelities of atom-to-photon teleportation for the four Bell measurement results, with and without correction.

state	fidelity w correction	fidelity w/o correction
$ \Phi^-\rangle$	84(8) %	83(8) %
$ \Phi^+\rangle$	86(7) %	85(7) %
$ \Psi^-\rangle$	77(12) %	66(6) %
$ \Psi^+\rangle$	76(8) %	69(5) %

$(|-\frac{5}{2}\rangle_D + e^{i\phi} |+\frac{5}{2}\rangle_D) / \sqrt{2}$ . The phase  $\phi$  oscillates due to the Larmor precession but is well defined in every absorption event by the detection time of the 393 nm herald. For each detection, the phase is determined and used as input phase of the run. After the teleportation protocol, state tomography on the 854 nm target photon B is applied. It consists in measuring the photon in the H/V, D/A, and R/L polarization bases, successively, for each atomic input state. The measurements are then used to reconstruct the quantum process matrix [32] in the Pauli basis  $\sigma_0, \sigma_x, \sigma_y, \sigma_z$  with a maximum likelihood algorithm. The result of the reconstruction is shown in figure 4. Conditioned on the eight possible outcomes of eqs. (9)-(12), we see that either a  $\sigma_x$ , a  $\sigma_y$ , a  $\sigma_z$ , or no rotation must be applied to the target photon to reveal the prepared input state. The corresponding entries in the process matrix are referred to as process fidelities; they are listed in table II. The mean process fidelity is 76(9) % (81(5) % with background and binning correction).

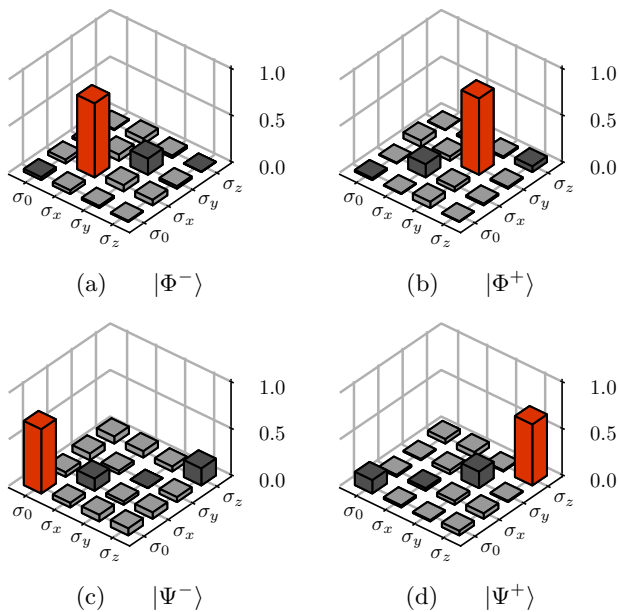


FIG. 4. Reconstructed process matrices of the quantum state teleportation conditioned on the Bell-state measurement results. (a) and (b) correspond to the  $|\Phi^-\rangle$  and  $|\Phi^+\rangle$  Bell states, (c) and (d) correspond to the  $|\Psi^-\rangle$  and  $|\Psi^+\rangle$  Bell states. Background and binning correction is applied.

## DISCUSSION AND CONCLUSION

The statistics of Fig. 4 are based on 511 670 886 executions of the teleportation protocol (i.e., coincident registration of the absorption herald and the partner photon) in 49.75 h hours of measurement. Given the free-space coupling between ion and in- and outgoing photons, the success probability for an individual heralded absorption event is on the order of  $1.04 \times 10^{-3}$  in the first passage, and  $1.32 \times 10^{-4}$  in the second passage; the partner photon is detected with 12.6 % probability. Detailed numbers are given in the supplement. Much higher rates will be expected when the absorption and the release of the herald are enhanced by optical resonators [33]. Nevertheless, the fidelity of the protocol is independent of the success probability, because the herald allows us to filter out successful events. Factors that limit the fidelity are polarization impurities in the optical paths, atomic decoherence due to magnetic noise, inherent background from the SPDC process, and the binning of the detected photon arrival times. The data of Fig. 4 and the fidelity numbers given in brackets are corrected for background and binning.

Comparing the measured entanglement transfer fidelity, table I, with what one expects from the initial two-photon state (Fig. 2) and the process fidelity of the mapping protocol, we note a few percent of deviation. The main reason for this are magnetic field fluctuations during the exposure of the ion to SPDC photons. We allowed up to 350  $\mu$ s for detecting a heralding photon. If we only use data from the first 50  $\mu$ s of exposure, then the fidelity  $\langle \Psi^- | \rho | \Psi^- \rangle$  increases from 78.0(9) % to 84(2) % (82.4(10) % to 89(2) %, with corrections) for the first passage. Due to the low signal and the correspondingly large uncertainty, the fidelity for the second passage does not change significantly.

In conclusion, we implemented several atom-photon interface operations between a single ion and resonant single photons from an SPDC entangled-pair source: mapping of a single-photon polarization qubit to a single-atom spin qubit, entanglement transfer from a photon-photon pair to an atom-photon pair, and quantum state teleportation from an atomic qubit to a photonic qubit. All operations are enabled by a heralded absorption – or single-photon Raman scattering – process; for the teleportation protocol, it serves as the Bell measurement, able to detect all four Bell states.

The interface operations illustrate how SPDC photon pair sources, as a resource of entanglement, and single atoms as quantum memories can be integrated in a quantum network. They also show the power of heralded operations that may reach high fidelities despite possibly low success probability.

In the future we will shift the photons from the ionic wavelength to the telecom wavelength range by quan-

tum frequency conversion [28], in order to benefit from low-loss, low-dispersion transmission over telecom fibers. This will allow us to apply our interfaces and establish remote entanglement for quantum repeater operations over an urban fiber link [34].

## METHODS

### Atomic manipulations

Coherent manipulations on the  $D_{5/2}$  and  $S_{1/2}$  Zeeman sub-levels of the ion are performed with a narrow-band 729 nm laser and a radio-frequency (RF) magnetic field antenna. To generate coherent superposition of the  $D_{5/2}$  Zeeman states, the ion is first initialized in the pure state  $|-\frac{1}{2}\rangle_S$  by Doppler cooling and frequency-selective optical pumping. Then a resonant  $\pi/2$  RF pulse is applied on the  $S_{1/2}$  Zeeman sub levels, and finally two 729 nm  $\pi$ -pulses transfer the population coherently to the  $D_{5/2}$  manifold. A set of 397 nm and 866 nm lasers is used for Doppler cooling on the  $S_{1/2}$ - $P_{1/2}$  transition, and for fluorescence detection. [9, 25]

### Larmor precession and spin echo

Due to the Zeeman splitting in the static magnetic field, the atomic superposition states undergo Larmor precession. The  $D_{5/2}$  superposition precesses with 24 MHz, whereas the  $S_{1/2}$  qubit oscillates at 8 MHz. We take advantage of the different Larmor precession frequencies and the variable waiting time until heralded absorption occurs, to provide atomic superposition states with different phases in each run. Our phase reference is an RF oscillator set to the Larmor frequency of the ground-state qubit. The phase of each event is calculated a posteriori from the arrival time of the absorption herald.

Fluctuations in the ambient magnetic field change the Larmor frequencies and give rise to phase errors. While slow variations (50 Hz and harmonics) are suppressed using a feed-forward stabilization via compensation coils, faster noise leads to decoherence of the atomic qubits. A spin-echo [35] technique compensates these errors partially: by applying a  $\pi$ -pulse on the ground-state qubit and a subsequent waiting time  $\tau_S = 3 \times \tau_D$  before projecting the atomic state, the phase error accumulated in  $D_{5/2}$  during the time  $\tau_D$  between preparation and absorption is corrected. The factor 3 in the waiting time is determined by the ratio between the Larmor frequencies of the  $D_{5/2}$  and the  $S_{1/2}$  Zeeman qubits.

Instead of triggering the spin-echo pulses directly by the herald, we check every 500 ns whether absorption has occurred. By choosing the loop time, and thereby also  $\tau_D$  and  $\tau_S$ , to be an integer multiple of the difference

of the two Larmor frequencies, we avoid fractional phase accumulation.

## ACKNOWLEDGEMENTS

We acknowledge support by the German Federal Ministry of Education and Research (BMBF) through projects Q.Link.X (16KIS0864), CaLas (13N14908), and QR.X (16KISQ001K).

\* juergen.eschner@physik.uni-saarland.de

- [1] Kimble, H. J. The quantum internet. *Nature* **453**, 1023 (2008).
- [2] Duan, L.-M. & Monroe, C. *Colloquium: Quantum networks with trapped ions*. *Rev. Mod. Phys.* **82**, 1209 (2010).
- [3] Briegel, H.-J., Dür, W., Cirac, J. I. & Zoller, P. Quantum repeaters: The role of imperfect local operations in quantum communication. *Phys. Rev. Lett.* **81**, 5932 (1998).
- [4] Brito, J., Kucera, S., Eich, P., Müller, P. & Eschner, J. Doubly heralded single-photon absorption by a single atom. *Appl. Phys. B* **122**, 36 (2016).
- [5] König, F., Mason, E. J., Wong, F. N. C. & Albota, M. A. Efficient and spectrally bright source of polarization-entangled photons. *Phys. Rev. A* **71**, 033805 (2005).
- [6] Rambach, M., Nikolova, A., Weinhold, T. J. & White, A. G. Sub-megahertz linewidth single photon source. *APL Photonics* **1**, 096101 (2016).
- [7] Tsai, P.-J. & Chen, Y.-C. Ultrabright, narrow-band photon-pair source for atomic quantum memories. *Quantum Sci. Technol.* **3**, 034005 (2018).
- [8] Bennett, C. H. *et al.* Teleporting an unknown quantum state via dual classical and einstein-podolsky-rosen channels. *Phys. Rev. Lett.* **70**, 1895–1899 (1993).
- [9] Kurz, C. *et al.* Experimental protocol for high-fidelity heralded photon-to-atom quantum state transfer. *Nat. Commun.* **5**, 5527 (2014).
- [10] Bouwmeester, D. *et al.* Experimental quantum teleportation. *Nature* **390**, 575–579 (1997).
- [11] Marcikic, I., de Riedmatten, H., Tittel, W., Zbinden, H. & Gisin, N. Long-distance teleportation of qubits at telecommunication wavelengths. *Nature* **421**, 509–513 (2003).
- [12] Landry, O., van Houwelingen, J. A. W., Beveratos, A., Zbinden, H. & Gisin, N. Quantum teleportation over the swisscom telecommunication network. *J. Opt. Soc. Am. B* **24**, 398–403 (2007).
- [13] Yin, J. *et al.* Quantum teleportation and entanglement distribution over 100-kilometre free-space channels. *Nature* **488**, 185–188 (2012).
- [14] Ma, X.-S. *et al.* Quantum teleportation over 143 kilometres using active feed-forward. *Nature* **489**, 269–273 (2012).
- [15] Ren, J.-G. *et al.* Ground-to-satellite quantum teleportation. *Nature* **549**, 70–73 (2017).
- [16] Riebe, M. *et al.* Deterministic quantum teleportation with atoms. *Nature* **429**, 734–737 (2004).

- [17] Olmschenk, S. *et al.* Quantum teleportation between distant matter qubits. *Science* **323**, 486–489 (2009).
- [18] Bao, X.-H. *et al.* Quantum teleportation between remote atomic-ensemble quantum memories. *Proc. Natl. Acad. Sci. U.S.A.* **109**, 20347–20351 (2012).
- [19] Nölleke, C. *et al.* Efficient teleportation between remote single-atom quantum memories. *Phys. Rev. Lett.* **110**, 140403 (2013).
- [20] Pfaff, W. *et al.* Unconditional quantum teleportation between distant solid-state quantum bits. *Science* **345**, 532–535 (2014).
- [21] Chen, Y.-A. *et al.* Memory-built-in quantum teleportation with photonic and atomic qubits. *Nat. Phys.* **4**, 103–107 (2008).
- [22] Sherson, J. F. *et al.* Quantum teleportation between light and matter. *Nature* **443**, 557–560 (2006).
- [23] Gao, W. *et al.* Quantum teleportation from a propagating photon to a solid-state spin qubit. *Nat. Commun.* **4**, 2744 (2013).
- [24] Bussières, F. *et al.* Quantum teleportation from a telecom-wavelength photon to a solid-state quantum memory. *Nat. Photon.* **8**, 775–778 (2014).
- [25] Kurz, C., Eich, P., Schug, M., Müller, P. & Eschner, J. Programmable atom-photon quantum interface. *Phys. Rev. A* **93**, 062348 (2016).
- [26] Schug, M. *et al.* Quantum interference in the absorption and emission of single photons by a single ion. *Phys. Rev. A* **90**, 023829 (2014).
- [27] Kurz, C. *Quantum networking with single ions and single photons interfaced in free space.* Ph.D. thesis, Saarland University (2015).
- [28] Arenskötter, E. *et al.* Telecom quantum photonic interface for a  $^{40}\text{Ca}^+$  single-ion quantum memory (2022). Preprint at <https://arxiv.org/abs/2211.08841>.
- [29] James, D. F. V., Kwiat, P. G., Munro, W. J. & White, A. G. Measurement of qubits. *Phys. Rev. A* **64**, 052312 (2001).
- [30] Müller, P. & Eschner, J. Single calcium-40 ion as quantum memory for photon polarization: a case study. *Appl. Phys. B* **114**, 303 (2014).
- [31] Kucera, S. *Experimental distribution of entanglement in ion-photon quantum networks : photon-pairs as resource.* Ph.D. thesis, Saarland University (2019).
- [32] Chuang, I. L. & Nielsen, M. A. Prescription for experimental determination of the dynamics of a quantum black box. *J. Mod. Opt.* **44**, 2455–2467 (1997).
- [33] Schupp, J. *et al.* Interface between trapped-ion qubits and traveling photons with close-to-optimal efficiency. *PRX Quantum* **2**, 020331 (2021).
- [34] Simon, C. *et al.* Quantum repeaters with photon pair sources and multimode memories. *Phys. Rev. Lett.* **98**, 190503 (2007).
- [35] Hahn, E. L. Spin echoes. *Phys. Rev.* **80**, 580–594 (1950).

## Supplementary information: Quantum teleportation with full Bell-basis detection between a $^{40}\text{Ca}^+$ ion and a single photon

Elena Arenskötter,<sup>1</sup> Stephan Kucera,<sup>1</sup> Omar Elshehy,<sup>1</sup> Max Bergerhoff,<sup>1</sup> Matthias Kreis,<sup>1</sup> and Jürgen Eschner<sup>1,\*</sup>

<sup>1</sup>*Experimentalphysik, Universität des Saarlandes, 66123 Saarbrücken, Germany*

(Dated: January 27, 2023)

### SINGLE-PHOTON TO ATOM QUANTUM STATE MAPPING

By pumping the SPDC resonator from only one side, we generate orthogonally polarized photon pairs, that are split on the polarizing beam splitter. We use the photon in arm A as the herald for a single photon in arm B, that is sent to the ion. The polarization of photon B is rotated to one of the 6 input polarizations  $|i\rangle \in \{|H\rangle, |D\rangle, |V\rangle, |A\rangle, |R\rangle, |L\rangle\}$ . We reconstruct the process matrix [1] by quantum state tomography on the final atomic state  $\rho_{f,i}$  for each input polarization. We correct the background for lost-partner events and detector dark counts.

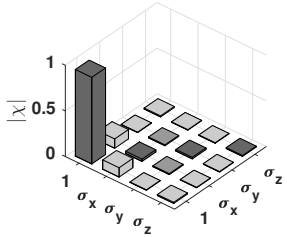


FIG. 1: Absolute values of the reconstructed process matrix with the identity part of 96.2 % and mean overlap fidelity of 96.7(8) %.

Figure 1 shows the absolute values of the process matrix  $\chi$  with the identity part of  $\chi_{11} = 96.2\%$  identified as the process fidelity. From this value, we infer the mean overlap fidelity  $\langle F \rangle = (2\chi_{11} + 1)/3 = 96.6\%$  (93.3% without background correction), which agrees with the mean of measured overlap fidelities of  $1/6 \sum_i \langle i | \rho_{f,i} | i \rangle = 96.7(8)\%$  (93(3)% without background correction). The major limitation is the coherence time of the ion due to magnetic field fluctuations during the exposure time of 56  $\mu\text{s}$ . We repeated the protocol  $1.13 \times 10^8$  times for the measurement, which led to a total exposure time of 1 h45 min. In this time, we generated  $9.3 \times 10^8$  heralded fibre-coupled 854 nm photons, and we recorded 7810 detected (background corrected) coincidences between the 854 nm herald and the emitted 393 nm photon. We extract the state mapping probability for a fiber coupled photon to be  $\eta = 8.4 \times 10^{-6}$ . Efficiencies for the entanglement transfer and the teleportation differ from these values and are discussed in the following sections.

### POLARISATION CONTROL

For setting the polarisation of photon B, we adjust the measurement basis at the detectors: we send laser light backwards through our setup and detect it with a polarimeter via a flip mirror. The rotation matrix of this flip mirror is compensated by three waveplates (quarter-wave, half-wave, quarter-wave). The projection setup generates 37 different input polarizations, equally distributed over the Poincare sphere. From the measured polarizations we then calculate the rotation matrix  $M_B$ .

The polarisation between the source and the trap is, in contrast, compensated behind the source: we insert a 99:1 fiber beam splitter in the fiber connecting source and trap. Between the source and the beam splitter we install a fiber polarisation controller (PolaRITE III PCD-M02-854), and between beam splitter and trap a 3-paddle polarisation controller. The 1 % output of the beam splitter is connected to a reference polarimeter. For calibration, we send a reference laser beam from the back-reflection direction. Its polarization is first adjusted to  $|R\rangle$  at the position of the ion, indicated by maximal suppression of the corresponding orthogonal transition. With an optional quarter-wave plate the reference polarization is rotated to  $|H\rangle$ . The next step is to compensate the polarisation to the reference polarimeter with the fiber paddles. In the next step we compensate the polarisation to the source, which is measured with an additional polarimeter in front of the source. The last step is to send the light from the source direction and compensate the polarisation of the back-reflection, measured again with the reference polarimeter.

### PHOTON-PHOTON TO ATOM-PHOTON ENTANGLEMENT TRANSFER: DATA AND EVALUATION

We perform a tomographic complete set of measurements to reconstruct the two-qubit ion-photon quantum state after heralded absorption,  $\rho$ . The chosen observables are the 16 tensor products  $\{\hat{\sigma}_i \otimes \hat{\sigma}_j | i, j = 0, \dots, 3\}$  of identity and Pauli spin operators  $\{\hat{\sigma}_{0,\dots,3}\} = \{\hat{1}, \hat{\sigma}_x, \hat{\sigma}_y, \hat{\sigma}_z\}$ . Their expectation values

$$\langle \hat{\sigma}_i \otimes \hat{\sigma}_j \rangle_\rho = \text{tr}(\hat{\sigma}_i \otimes \hat{\sigma}_j \rho) \quad (1)$$

allow for direct reconstruction of  $\rho$  by linear combination

$$\rho = \frac{1}{4} \sum_{i,j=0}^3 \langle \hat{\sigma}_i \otimes \hat{\sigma}_j \rangle_{\rho} \cdot \hat{\sigma}_i \otimes \hat{\sigma}_j \quad (2)$$

We write the expectation values as

$$\langle \hat{\sigma}_i \otimes \hat{\sigma}_j \rangle = \lambda_{|0_i\rangle} \cdot P(|0_i\rangle) \cdot \langle \hat{\sigma}_j \rangle \Big|_{|0_i\rangle} + \lambda_{|1_i\rangle} \cdot P(|1_i\rangle) \cdot \langle \hat{\sigma}_j \rangle \Big|_{|1_i\rangle} \quad (3)$$

where  $\lambda_{|0_i\rangle}$ ,  $\lambda_{|1_i\rangle}$  denote the eigenvalues of the observables  $\hat{\sigma}_i$  of the photonic qubit,  $P(|0_i\rangle)$  and  $P(|1_i\rangle)$  are the probabilities to detect the photonic qubit in the eigenstates  $|0_i\rangle$  and  $|1_i\rangle$  of this observable, and  $\langle \hat{\sigma}_j \rangle \Big|_{|0_i\rangle}$  and  $\langle \hat{\sigma}_j \rangle \Big|_{|1_i\rangle}$  are the conditioned expectation values of the atomic qubit after detection of the photonic qubit in the eigenstate  $|0_i\rangle$  respectively  $|1_i\rangle$ .

The photonic projection in the basis settings  $|H\rangle/|V\rangle$ ,  $|D\rangle/|A\rangle$ , and  $|R\rangle/|L\rangle$  is performed with a set of quarter-wave and half-wave plate and two APDs at the output of a polarizing beam splitter. For the atomic projection onto the  $|\pm\frac{1}{2}\rangle_S$  basis, i.e. for  $\langle \hat{\sigma}_z \rangle$ , we perform electron shelving and fluorescence detection. An additional  $\pi/2$  RF pulse before electron shelving is used to project onto the superposition basis. Atomic superpositions carry a Larmor precession phase defined by the time instant at which the heralded absorption happened. We therefore plot the projection result after the  $\pi/2$  pulse as a function of this Larmor phase and extract  $\langle \hat{\sigma}_{x,y} \rangle$  from a fit to a sinusoidal function

$$\frac{V}{2} \sin(x - \phi_0) + \frac{1}{2} \quad . \quad (4)$$

If we correct for the influence of the binning, the fit function changes to

$$\frac{V}{2} \frac{N}{\pi} \sin\left(\frac{\pi}{N}\right) \sin(x - \phi_0) + \frac{1}{2} \quad (5)$$

with the number of bins  $N$ .

Figure 2 and 3 show the atomic state analysis under condition of the six different 854 nm projector settings with and without  $\pi/2$  RF pulse. The gray fringes and bars are without background correction. Out of this dataset we calculate the conditioned expectation values of the atomic qubit.

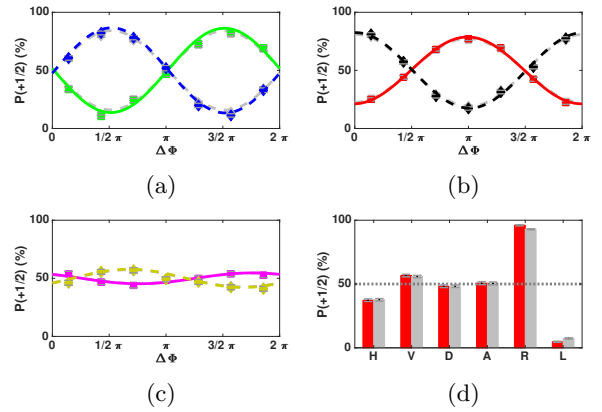


FIG. 2: (a-c) Fringes (with basis rotation) for the six projector settings of the first passage and the 854 nm partner photon. The gray dashed lines show the data without correction:

- (a) green (squares):  $|H\rangle$ , blue (diamonds):  $|V\rangle$
- (b) red (squares):  $|D\rangle$ , black (diamonds):  $|A\rangle$
- (c) magenta (squares):  $|R\rangle$ , yellow (diamonds):  $|L\rangle$
- (d) Probabilities (without  $\pi/2$  RF pulse) for the six projector settings of the 854 nm partner photon (red bars). The gray bars are without correction.

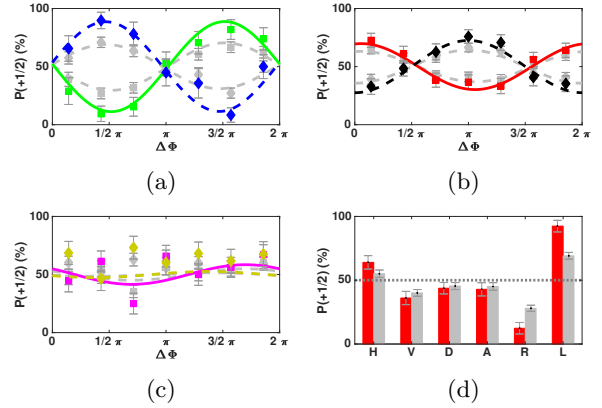


FIG. 3: (a-c) Fringes (with basis rotation) for the six projector settings of the second passage and the 854 nm partner photon. The gray dashed lines show the data without correction:

- (a) green (squares):  $|H\rangle$ , blue (diamonds):  $|V\rangle$
- (b) red (squares):  $|D\rangle$ , black (diamonds):  $|A\rangle$
- (c) magenta (squares):  $|R\rangle$ , yellow (diamonds):  $|L\rangle$
- (d) Probabilities (without basis rotation) for the six projector settings of the 854 nm partner photon (red bars). The gray bars are without correction.

## QUANTUM STATE TELEPORTATION: DATA AND EVALUATION

For the teleportation measurement, we calculate histograms of the correlated events of Bell-state measurements and partner-photon polarization. Figure 4 contains the teleportation measurement data. The columns correspond to the Bell-state-measurement outcome. The first three rows show the probabilities for the superposition input to detect  $|H\rangle_B$ ,  $|D\rangle_B$ , and  $|R\rangle_B$  in dependence of the superposition phase. The probabilities to detect  $|V\rangle_B$ ,  $|A\rangle_B$ , and  $|L\rangle_B$  are derived by calculating  $1 - P(\phi)_{(H/D/L)}$ . The last two rows contain the probabilities when starting with the energy eigenstates  $|\pm 5/2\rangle_D$ .

All probabilities are fed into a maximum likelihood algorithm to reconstruct the process matrix.

## QUANTUM STATE TELEPORTATION: RATES AND EFFICIENCIES

In total we performed  $N_{run} = 511\,670\,886$  measurement runs with  $\tau_{exp} = 350\,\mu\text{s}$  exposure time per run and recorded  $N_{c,\text{first}} = 89\,838$  coincident events between the 393 nm heralds and the 854 nm photons for the first passage and  $N_{c,\text{second}} = 11\,322$  for the second passage. The success probabilities per exposure time are then

$$\eta_{\text{success,run,first}} = \frac{N_{c,\text{first}}}{N_{run}} = 1.76 \times 10^{-4} \quad (6)$$

$$\eta_{\text{success,run,second}} = \frac{N_{c,\text{second}}}{N_{run}} = 2.21 \times 10^{-5} \quad (7)$$

The total exposure time  $T_{\text{tot,exposure}}$  was  $N_{run} \cdot \tau_{exp} = 1.79 \times 10^5\,\text{s} = 49.75\,\text{h}$ . With our pair rate per pump power of  $5.17 \times 10^4\,(\text{mW})^{-1}$  and 15 mW pump power we get the total number of generated pairs  $N_{\text{pairs}} = 1.388\,803 \times 10^{11}$ . The success probabilities per pair are then

$$\eta_{\text{success,pair,first}} = \frac{N_{c,\text{first}}}{N_{\text{pair}}} = 6.47 \times 10^{-7} \quad (8)$$

$$\eta_{\text{success,pair,second}} = \frac{N_{c,\text{second}}}{N_{\text{pair}}} = 8.15 \times 10^{-8} \quad (9)$$

These values are composed of several contributions. The detection efficiency of the 854 nm photons in arm B including APD quantum efficiency, spectral filters, fibers and all other optical components is  $\eta_{854,B} = 12.6\%$ . The total coupling efficiency from the photon-pair source to the ion setup (in front of the vacuum chamber) is  $\eta_{854,A} = 30\%$ . For detecting the 393-nm absorption herald, the HALO covers 4% solid angle; in combination with the emission pattern of  $\sigma$ -transition it collects 6% of the emitted 393 nm photons. The 393 nm photon detection efficiency after the HALO is 37.5%. The total 393 nm detection efficiency is then  $\eta_{393} = 1.64\%$ .

We include coincidences between absorption herald and arm B photon within a gate of  $\pm 84\,\text{ns}$ , corresponding to  $\eta_{\text{gate}} = 99.9\%$  of the 854 nm photon wave packet. The remaining part is the absorption efficiency  $\eta_{\text{abs}}$  per incoming photon. We calculate these probabilities as

$$\eta_{\text{abs,first}} = \frac{\eta_{\text{success,pair,first}}}{\eta_{854,A} \eta_{854,B} \eta_{393} \eta_{\text{gate}}} = 1.04 \times 10^{-3} \quad (10)$$

$$\eta_{\text{abs,second}} = \frac{\eta_{\text{success,pair,second}}}{\eta_{854,A} \eta_{854,B} \eta_{393} \eta_{\text{gate}}} = 1.32 \times 10^{-4} \quad (11)$$

The absorption probability per photon is in good agreement with earlier measured values [2–4].

## QUANTUM STATE TELEPORTATION: ERROR BUDGET & IMPROVEMENTS

To investigate the influence of the magnetic field fluctuation, we vary the offset of the detection window (50  $\mu\text{s}$ ), taking only later events into account. The data is shown in Fig. 5. We see a linear decrease in fidelity. Therefore we claim that the fidelity is mainly limited by decoherence due to magnetic field fluctuations.

One improvement, especially for the entanglement transfer, is to avoid the influence of the Larmor phase. To describe the qubit without this phase we need to deal with the different energy spacings of the qubits. This can be done by simultaneously changing the frequency of the reference oscillator to the Larmor frequency of the D-state qubit, while the electron is in the D-state. Once the herald of absorption is detected, the frequency is changed back to the Larmor frequency of the ground-state qubit. In this way, the reference oscillator is always in phase.

## Supplementary References

---

\* juergen.eschner@physik.uni-saarland.de

- [1] Chuang I. L., Nielsen, M. A. (1997) Prescription for experimental determination of the dynamics of a quantum black box. *Journal of Modern Optics* 44(11-12):2455-2467 <https://doi.org/10.1080/09500349708231894>
- [2] Brito J., Kucera S., Eich P., Müller P., Eschner J. (2016) Doubly heralded single-photon absorption by a single atom. *Appl. Phys. B* 122(36) <https://doi.org/10.1007/s00340-015-6276-9>
- [3] Lenhard A., Bock M., Becher C., Kucera S., Brito J., Eich P., Müller P., Eschner J. (2015) Telecom-heralded single-photon absorption by a single atom. *Phys. Rev. A* 92(063827) <https://doi.org/10.1103/PhysRevA.92.063827>
- [4] Kucera S. (2019) Experimental distribution of entanglement in ion-photon quantum networks : photon-pairs as

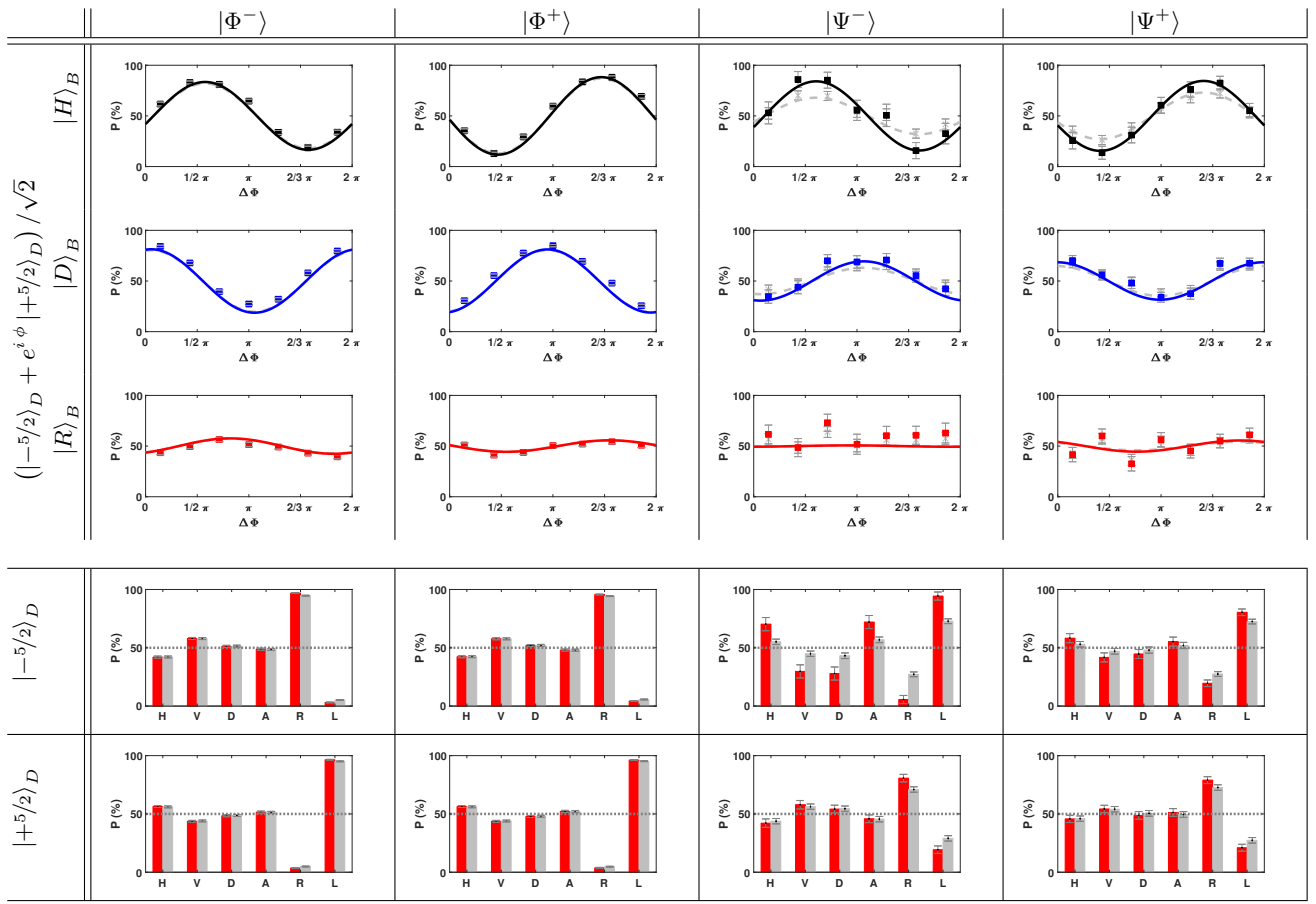
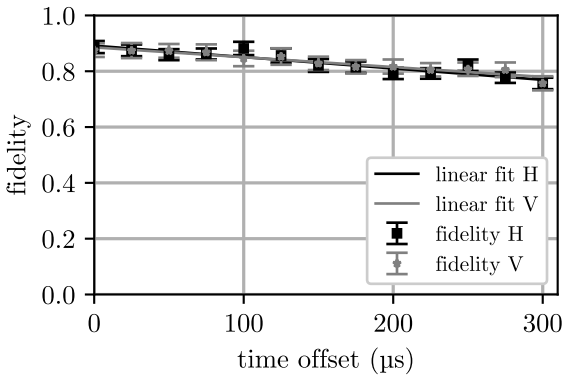


FIG. 4: Teleportation measurement data evaluated for a exposure time of 350  $\mu$ s. Gray bars and lines show the data without correction. The coloured ones with correction.



resource. Dissertation, Universität des Saarlandes <https://dx.doi.org/10.22028/D291-28393>

FIG. 5: Atom-photon fidelity depending on the time offset for a fixed detection window of 50  $\mu$ s